



3D printing of customized MnO₂ cathode for aqueous zinc-ion batteries

Zhen LIU¹, Han-bing HE¹, Ze-xiang LUO¹, Xiao-feng WANG², Jing ZENG¹

1. School of Metallurgy and Environment, Central South University, Changsha 410083, China;

2. School of Materials Science and Engineering, Central South University, Changsha 410083, China

Received 13 January 2022; accepted 27 April 2022

Abstract: In order to overcome the problems of inferior cycling stability and slow ion diffusion of MnO₂ cathode in aqueous zinc-ion battery, a high-accuracy customized 3D printed MnO₂ cathode was prepared via direct ink writing. The rheological test showed that the printing ink indicated shear-thinning behavior with the storage modulus platform value over 10⁵ Pa. The SEM images displayed that the customized mesh-layer structure was well maintained after 100 cycles. The 3D structure with excellent mechanical strength could effectively alleviate the internal stress and provide a greater specific surface area. The specific capacity of the 3D printing cathode was three times higher than that of the 2D one at 50 mA/g after 110 stable cycles. The energy storage mechanism of the reversible Mn²⁺/Mn⁴⁺ double redox for 3D printing battery was also studied through a variety of ex-situ experiments.

Key words: α -MnO₂; aqueous zinc-ion batteries; 3D printing; direct ink writing; energy storage mechanism

1 Introduction

Aqueous zinc-ion battery (ZIB) is one of the most promising rechargeable batteries due to its environmental friendliness and high energy density [1–3]. Currently, the cathode materials of ZIBs consist of Prussian blue analogs, vanadium-based oxides, organic compounds and manganese-based oxides [4–6]. Among them, manganese oxides have been intensively researched owing to their diverse crystal structures (α -MnO₂, β -MnO₂, γ -MnO₂, MnO, Mn₃O₄, etc.) and ultrahigh theoretical specific capacity [7,8]. However, the irreversible structural transformation and the dissolution of Mn²⁺ during charge/discharge process cause capacity attenuation of the battery [9].

Until now, element doping and surface coating have been the main methods to solve such problems [10,11]. However, elemental doping reduces the active ingredients and the gravimetric

capacity, and some of the coating can hinder the ion transport [12,13]. Besides, traditional coating electrodes have constraints in controlling the spatial structure and geometry of the electrodes, and the limited electrolyte penetration leads to slow ion transport, which affects the charge storage performance [14,15]. In order to increase the areal capacitance and energy density of the 2D electrode, it is necessary to raise the active material load, that is, to construct a thicker electrode, which inevitably increases the ion transmission distance and total resistance [16].

Therefore, compared with the traditional coating electrode, the 3D printing electrode not only provides a lower resistance and shorter diffusion path during ion transmission process, but also makes full use of the limited space and creates a porous structure to increase the energy density significantly [17,18]. Most 3D printed batteries are based on inkjet printing (IJP). For instance, WANG et al [19] combined inkjet printing with stamping

Corresponding author: Han-bing HE, Tel: +86-13875985605, E-mail: hehanbinghbb@csu.edu.cn;

Jing ZENG, Tel: +86-15116335400, E-mail: zengjing@csu.edu.cn

DOI: 10.1016/S1003-6326(23)66175-8

1003-6326/© 2023 The Nonferrous Metals Society of China. Published by Elsevier Ltd & Science Press

metal film-printed metal patterns and constructed Zn/MnO₂ batteries with a great cycle capacity of 253 mA·h/g at 500 mA/g for 50 cycles. Besides, stereolithography (SLA) is also used in the fabrication of electrochemical storage equipment. ZHANG et al [20] developed a technique of electroless deposition combined with 3D printing to fabricate a Zn anode. And the battery delivered a high capacity retention (80%) at 10 A/g after 1000 cycles. However, IJP and SLA have to combine with other technologies, instead of completing the task independently, which will increase the additional cost in production. And these methods are difficult to meet the requirements of high precision.

Nevertheless, direct ink writing (DIW) can solve the above problems at the same time due to its simple operation and the ability to transform any shape designed by digital technology into a high-precision solid 3D model [21,22]. Hence, we prepared a cathode material for zinc manganese batteries by 3D DIW. Compared with traditional coating electrodes, 3D printing electrodes have a higher solid–liquid interface area, and the mesh-layered structure will deal with the problems of volume expansion/contraction and thermal diffusion. At present, DIW is mainly studied in the solid-state electrolytes manufacturing of lithium-ion batteries. LIU et al [23] directly printed the LATP-based hybrid solid-state electrolytes on LiFePO₄ cathodes for lithium-ion batteries with the discharge capacity of 150 mA·h/g at 0.5C. However, it was barely reported on the application of DIW in zinc ion batteries. Therefore, this designable electrode preparation method provides a novel idea for the further application of ZIBs.

2 Experimental

2.1 Preparation of α -MnO₂

The manganese oxides were synthesized by a coprecipitation method. Briefly, 1.5 g of KMnO₄ was first dispersed into 73.5 mL of deionized (DI) water to obtain Solution A. 0.34 g C₄H₆MnO₄·4H₂O was dissolved in 9.6 mL of DI water to obtain Solution B. Then, Solution A was added dropwise to Solution B under magnetic stirring. The suspension was stood for 2 h and then rinsed with DI water and ethanol several times. After drying at 60 °C for 12 h, MnO₂ was obtained.

2.2 Preparation of traditional coating electrode

The active material, conductive agent and binder (coprecipitated MnO₂, acetylene black and PVDF, respectively) were mixed with a mass ratio of 7:2:1. Next, a proper quantity of N-methylpyrrolidone (NMP) was added to form a slurry. Then, the slurry was coated on the stainless-steel foil evenly and dried in the vacuum oven at 100 °C for 12 h.

2.3 Preparation of 3D printing electrode

0.2 g acetylene black and 0.7 g coprecipitated MnO₂ were added in the agate mortar. The Mixture C was obtained by grounding the mixture for 25 min. PVDF (0.1 g) and an appropriate amount of NMP were added to a mixing bottle. And then, the bottle was kept in the oven at 60 °C for 15 min to obtain transparent Solution D. Finally, Mixture C and Solution D were fully mixed with the planetary mixer.

Firstly, the stainless-steel foil was fixed on the printing platform. The syringe with ink was then assembled on the direct-write molding instrument, and the print parameters were set as follows: the extrusion pressure was 275.8 kPa, and the printing speed was 2.5 mm/s. Finally, the product was put into the vacuum oven at 100 °C for 12 h. In addition, the complete process of the 3D printing electrode preparation is shown in Fig. 1. And the optimizing process of 3D printing parameters is shown in Fig. S1 in Supporting Materials.

2.4 Material testing

X-ray diffraction (XRD) patterns were recorded on the PANalytical Empyrean 2 diffractometer of Netherlands. X-ray photoelectron spectroscopy (XPS) spectra were recorded by the Thermo Scientific K-Alpha spectrometer of America with a monochromatic Al K _{α} X-ray source. Scanning electron microscopy (SEM) images were recorded by the JSM–7900F microscope of Japan. Rheological properties and viscoelastic properties were measured by the TA AR2000EX of Britain.

2.5 Electrochemical testing

Electrochemical performance tests were executed using 2025-type coin cells with metallic zinc foil as a counter electrode. In addition, the electrolyte was composed of 0.3 mol/L MnSO₄ and 1 mol/L ZnSO₄ solution. The discharge/charge

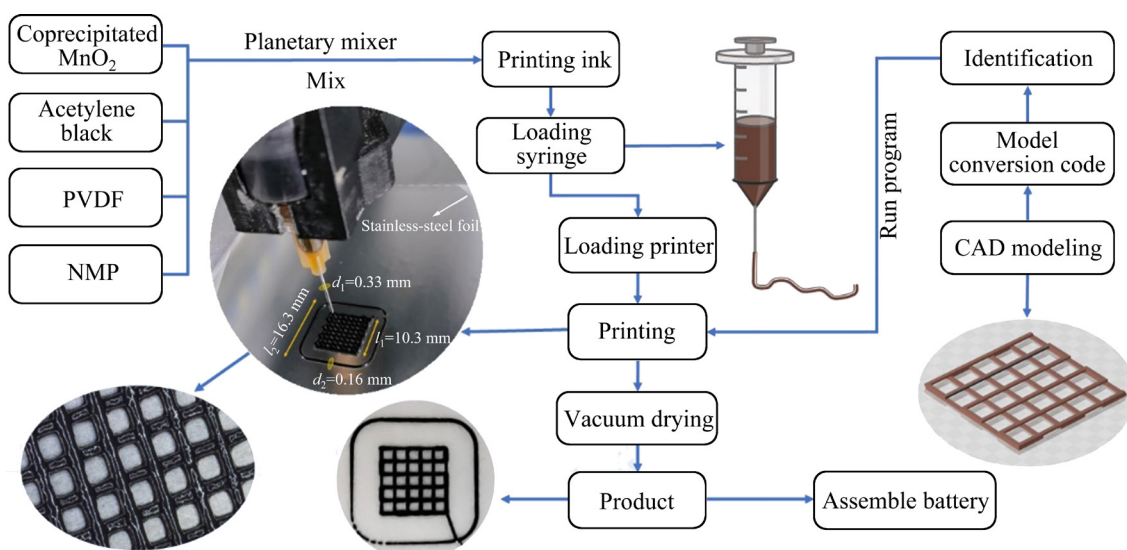


Fig. 1 Schematic diagram of 3D printing process and photograph of printed product

experiments were recorded by the LANHE Testing System (CT3001A, Wuhan, China), and the potential window was 0.8–1.8 V. The cyclic voltammograms (CV) were tested on the CHI600E electrochemical workstation. The electrochemical impedance spectra (EIS) were obtained on the MULTI AUTOLAB M204 impedance analyser.

3 Results and discussion

3.1 Material characterization

The phase composition and crystal structure of coprecipitated MnO_2 were analyzed by XRD. The diffraction peaks of manganese oxide powder corresponded to the (110), (310), (211) and (521) planes of $\alpha\text{-MnO}_2$ (JCPDS No. 44-0141), as shown in the XRD pattern (Fig. 2(a)).

The manganese valence state of $\alpha\text{-MnO}_2$ was analyzed by XPS. In Fig. 2(b), four peaks were shown by the 2p orbital high-resolution spectrum of Mn, which corresponded to Mn^{4+} and Mn^{3+} at 642.4 eV (653.2 eV) and 640.9 eV (652.3 eV), respectively [24]. Therefore, the $\alpha\text{-MnO}_2$ prepared by the coprecipitation method contained a small amount of Mn_2O_3 impurity, and the content of Mn_2O_3 was approximately 18.3% (Table S1 in Supporting Materials).

A nanorod structure with typical $\alpha\text{-MnO}_2$ morphology was observed in the TEM images of $\alpha\text{-MnO}_2$ (Figs. 3(a, b)). Nanorods of 100–200 nm had a wide particle size distribution, which could better contact each other during the extrusion process and increase the solid volume fraction of

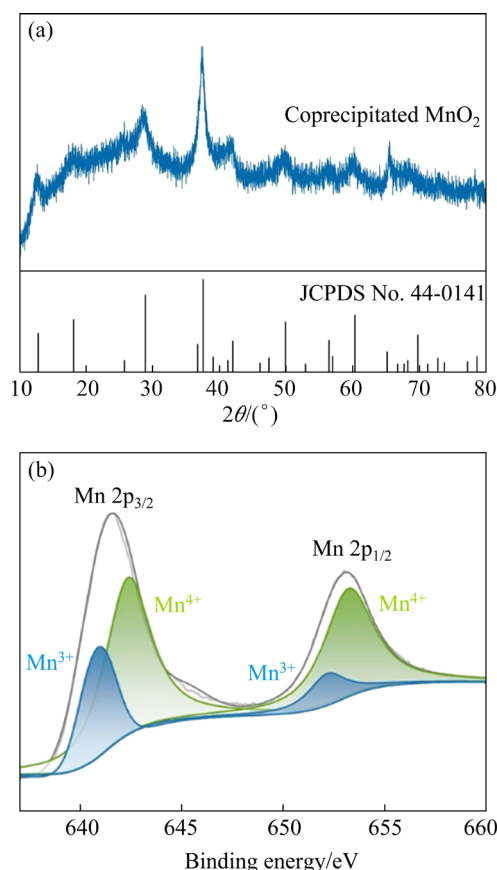


Fig. 2 XRD pattern (a) and XPS spectra (b) of $\alpha\text{-MnO}_2$

the inks (Fig. S2 in Supporting Materials). Clear and regular lattice fringes were observed in the HRTEM image (Fig. 3(c)). And the spacing of 0.342 nm corresponded to the (211) crystal plane of $\alpha\text{-MnO}_2$. A small amount of K was observed through energy-dispersive X-ray (EDX) elemental mapping images (Fig. 3(d)), indicating K ions were

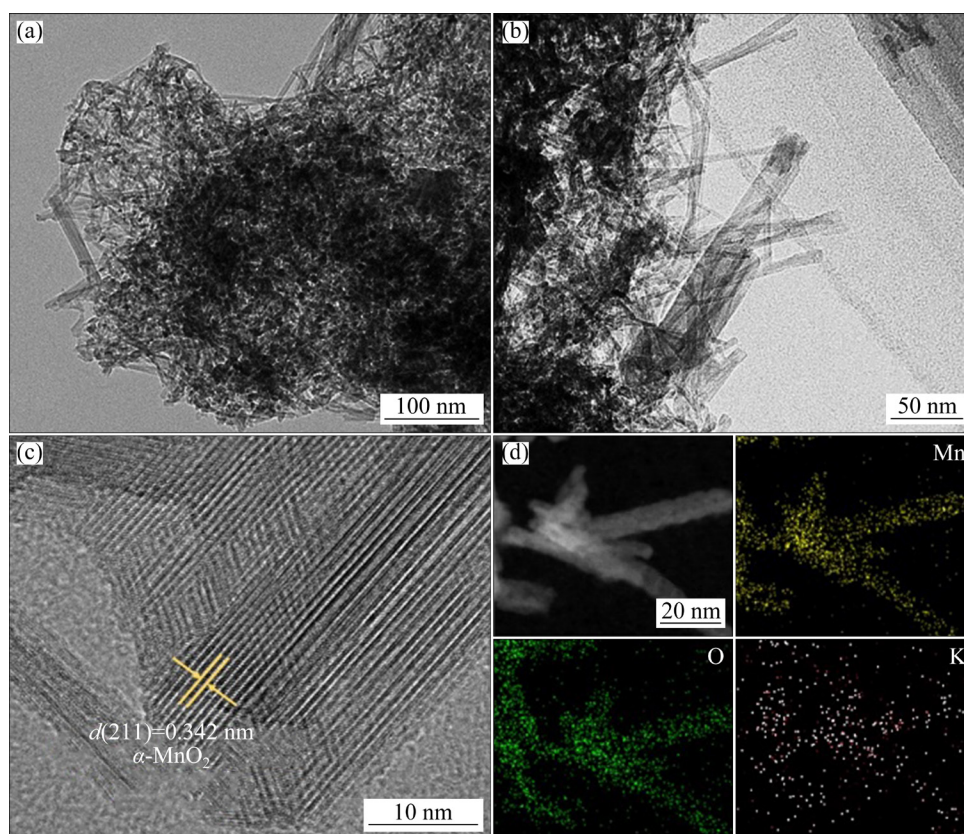


Fig. 3 TEM image (a, b), HRTEM image (c), and EDX elemental mapping images (d) of α -MnO₂

successfully doped into α -MnO₂ during the synthesis process, which was beneficial to maintaining the morphology of α -MnO₂ [25].

The SEM image (Fig. 4(a)) shows that the coprecipitated MnO₂ aggregates with sizes of 0.5–1.0 μ m were composed of nanorods with lengths of 100–200 nm. As shown in Fig. 4(b), the MnO₂ of the traditional coating electrode was uniformly distributed in the binder and the conductive agent was in the form of small particles. After 100 cycles, the surface of the electrode was obviously cracked, and the exposed MnO₂ particles grew slightly (Fig. 4(c)). The photographs of the 3D printing electrode before drying are shown in Figs. S3 and S4 in Supporting Materials. As shown in Figs. 4(d, e), the dry 3D printing electrode maintained a well mesh-layered structure. After 100 cycles, the surface of the electrode became rougher as the exposed MnO₂ grew into a block morphology (Fig. 4(i)). In addition, the 3D structure was well maintained, which proved that the ink had excellent mechanical strength after drying (Figs. 4(g, h)).

The rheological test was used to determine whether the ink met the requirement of 3D printing.

As shown in Fig. 5(a), with the increase of shear rate, the ink appeared shear-thinning behaviour, which proved that the ink was a typical non-Newtonian fluid. The apparent viscosity of fresh ink was 2818.1 Pa·s, when the shear rate was 0.1 s⁻¹, and the apparent viscosity decreased to the order of 10 Pa·s when the shear rate was 100 s⁻¹. This phenomenon proved that the ink had good fluidity at a certain shear rate [26,27]. Besides, the initial apparent viscosity of the ink after 24 h was slightly lower than that of the fresh ink, and with the increase of shear rate, its apparent viscosity was almost the same as that of the fresh ink.

Figure 5(b) shows that the fresh ink had a stable long plateau period, which was dominated by the storage modulus before the shear stress reached 1 $\times 10^3$ Pa. The storage modulus in the plateau period reached an order of 10⁵, which proved that the ink had a strong ability to resist shear force and maintain elastic deformation [28,29]. The initial storage modulus of the ink after 24 h (Fig. 5(c)) was slightly lower than that of the fresh ink, and the other rheological behaviors were the same as those of the fresh ink on the whole, which proved that the ink had good dispersion stability.

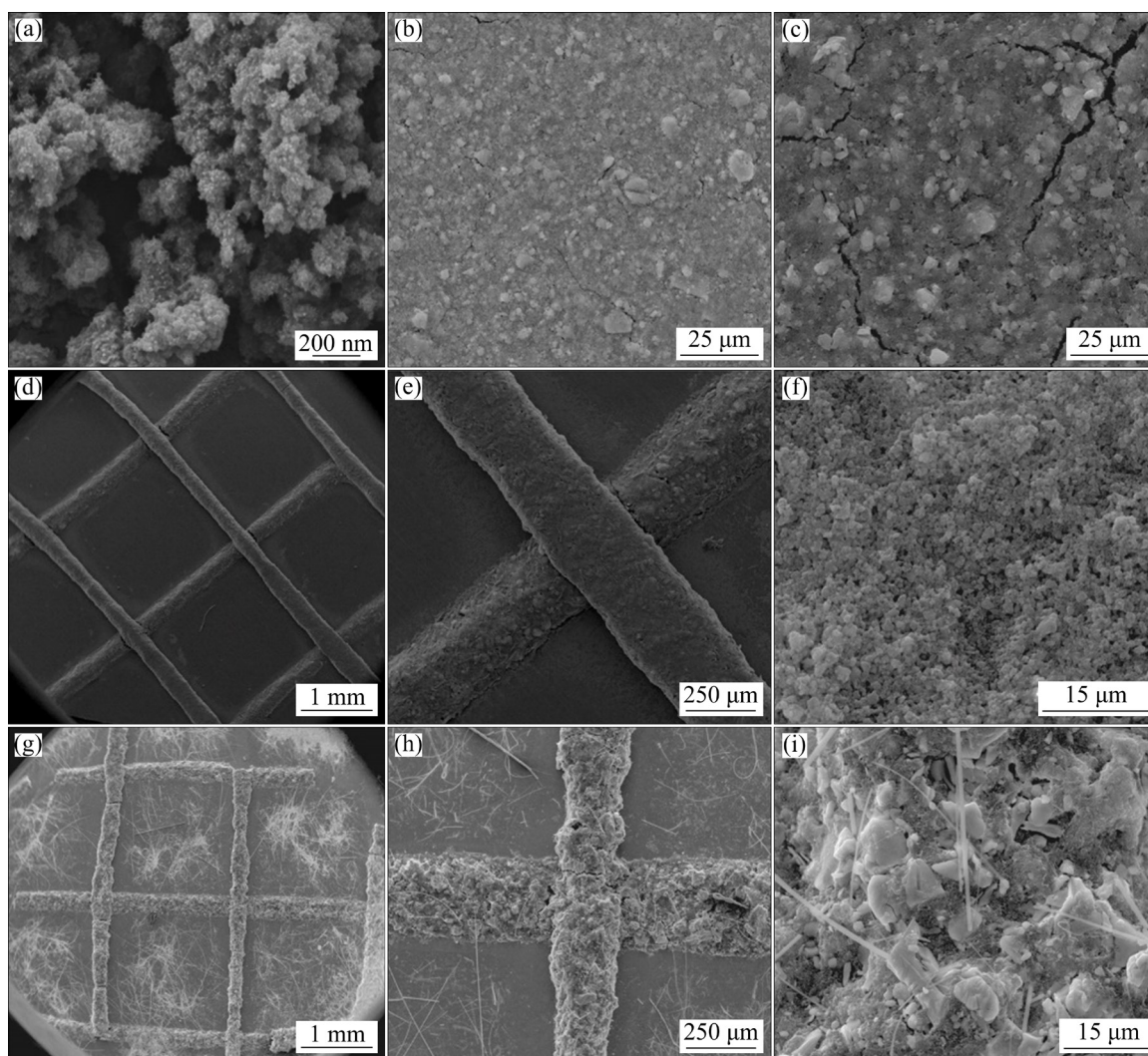


Fig. 4 SEM images: (a) Material characterizations of coprecipitated MnO_2 ; (b) Traditional coating electrode before cycling; (c) Traditional coating electrode after 100 cycles; (d–f) 3D printing electrode before cycling; (g–i) 3D printing electrode after 100 cycles

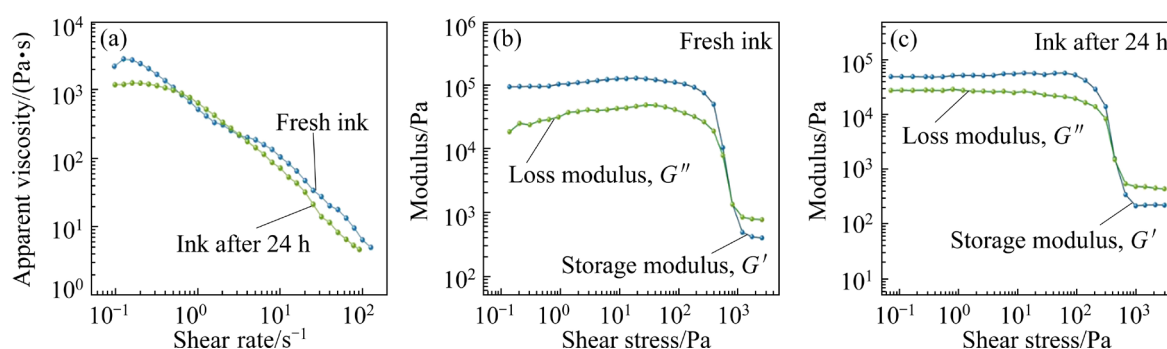


Fig. 5 Apparent viscosity as function of shear rate (a), and storage modulus (G') and loss modulus (G'') (b, c) of ink

Figures 6(a, b) display the initial three cycles of cyclic voltammetry (CV) corresponding to the traditional coating battery and 3D printing battery. The voltage range was 0.8–1.8 V (vs Zn/Zn^{2+}) with the scan rate as 0.1 mV/s. Several pairs of redox

peaks were observed in these curves, which was due to the extraction/insertion of Zn^{2+} ions in MnO_2 . In general, the CV curves of two sets of batteries had good repeatability except that the first lap was slightly biased in generating the SEI film.

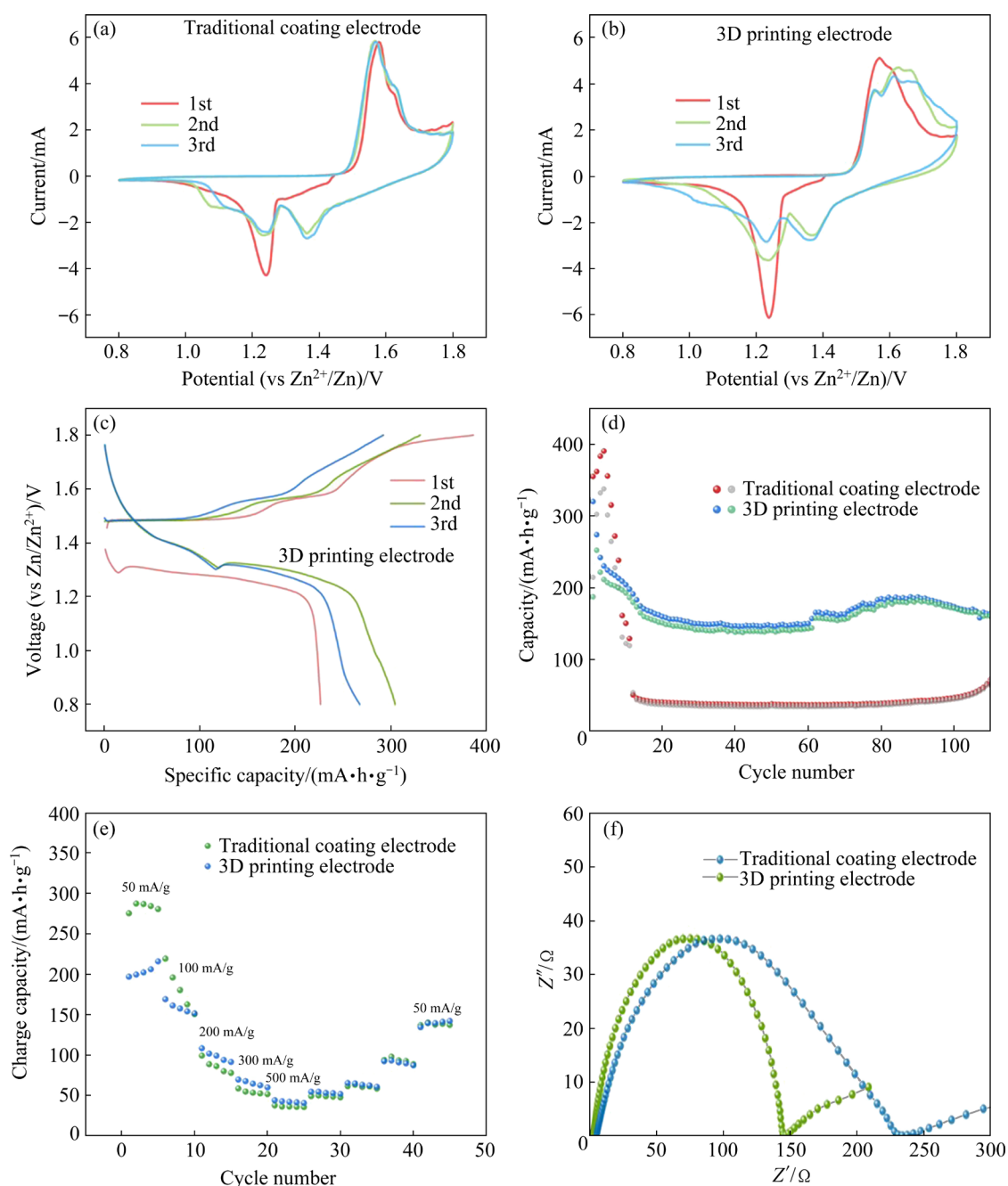
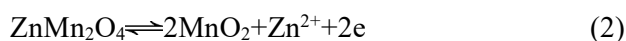
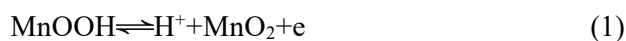


Fig. 6 CV curves of traditional coating electrode (a) and 3D printing electrode (b) at 0.1 mV/s; Cyclic performance of traditional coating electrode and 3D printing electrode at 50 mA/g (c, d); Rate performance of traditional coating electrode and 3D printing electrode (e); EIS spectra of traditional coating electrode and 3D printing electrode (f)

The current response at 1.23 V was related to the formation of ZnMn_2O_4 or MnOOH during the initial process of cathodic polarization. In addition, the traditional coating battery had a weak current response between 1.0 and 1.1 V owing to the occurrence of side reactions, which was not found in 3D printing batteries. In the initial anodic sweep, a current response of the traditional coating battery was observed at 1.57 V, while the current of the 3D printing battery continued to respond within

1.5–1.7 V. This result indicated that the extraction process of H^+ and Zn^{2+} was carried out continuously over a wide voltage range [30]. The reactions could be formulated as follows:



The electrochemical cycle of the traditional coating battery at 50 mA/g is shown in Fig. S5 in Supporting Materials. On the first discharge curve,

two platforms located at 1.3–1.35 V and 0.86–0.95 V were observed, which were interrelated with the formation of spinel ZnMn_2O_4 or monoclinic MnOOH in the initial process of cathodic polarization. However, the 3D printing battery only had a plateau at 1.2–1.3 V and was smoother than the traditional battery, which further proved that the H^+ and Zn^{2+} extraction/insertion process in the 3D printing battery was more continuous and stable (Fig. 6(c)).

The cycling performances of the traditional coating battery and 3D printing battery at 50 mA/g were compared in Fig. 6(d). A sharp capacity decay was observed on the curve of the traditional battery, and the capacity decreased to 40 mA·h/g after 20 cycles, while the capacity of the 3D printing battery stabilized at 150 mA·h/g. This demonstrated that the 3D printing structure was conducive to the maintenance and stability of the capacity.

Moreover, the rate capabilities were contrasted at several current densities (Fig. 6(e)). As the current density raised from 50 to 500 mA/g, the capacities of the traditional coating battery were 280.6, 150.5, 77.9, 51.6, and 35.6 mA·h/g. Meanwhile, the capacities of the 3D printing battery were 215.9, 151.6, 91.4, 60.0, and 40.7 mA·h/g, which were slightly higher than those of the traditional battery and showed better recovery performance when returned to a low current density.

Nyquist plots of the traditional coating battery and 3D printing battery were compared in Fig. 6(f). The charge transfer resistance of the 3D printing battery was much smaller than that of the other

batteries, proving that the 3D printing structure gave a higher contact area between the electrolyte and active material, which was beneficial to charge transfer and ion diffusion.

3.2 Reaction mechanism

To improve the printing effect, the pressure filtration effect was used to assist the extrusion process. Since NMP is a Newtonian fluid, under the action of solvent pressure p_0 in evenly distributed pores, the ink has a pressure filter effect, and the filtered solvent penetrates from the ink, which satisfies Darcy's law:

$$v=q/A \quad (3)$$

$$q = \frac{\pi r_1^4}{8\eta} JtN \quad (4)$$

where v is the flow rate; q is the pressure filtration capacity; A is a cylindrical surface passing through during the pressure filtration process; r_1 is the radius of the void hole, which gradually decreases in the process of pressure filtration; J is the pressure gradient in the void hole; η is the viscosity coefficient of NMP; t is the time of pressure filtration; N is the void number on the calculated section.

Therefore, the pressure filtration effect was used to provide a self-lubricating effect in the needle by adjusting the needle diameter and extrusion pressure through the formula. In addition, part of the solvent was separated from the ink when the pressure filtration effect occurs, and the shrinkage of the 3D printing electrode after drying would be abated by reducing the solid volume fraction (Fig. 7(a)).

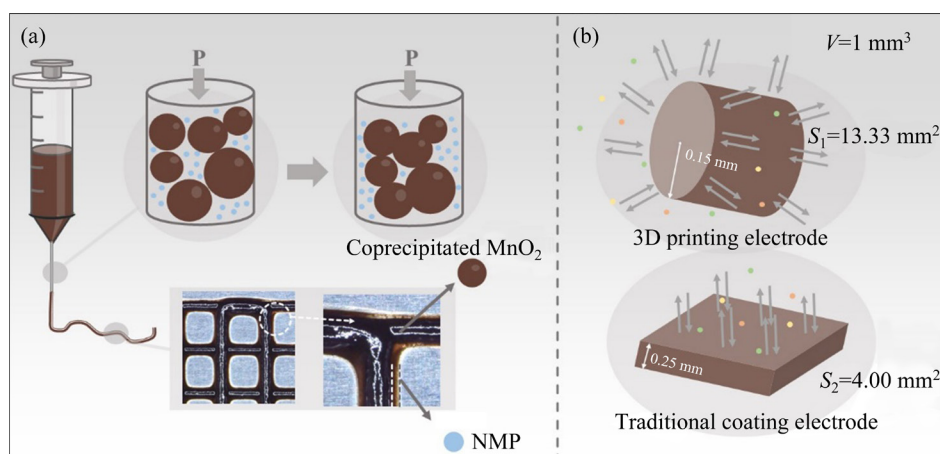


Fig. 7 Schematic diagram of pressure filtration effect (a) and comparison model of surface ion diffusion per unit volume (b)

Next, through the ex-situ XRD, ex-situ XPS, and ex-situ SEM, the morphology and crystal structure evolution were further explored. From the 5th cycle, such XRD patterns of the cathode under several charge/discharge states are compared in Fig. 8(a). It was observed that the peaks of $\text{Zn}_4\text{SO}_4(\text{OH})_6 \cdot 5\text{H}_2\text{O}$ (ZSH) were strong at 0.80 V. With the deepening of the charging, the peaks of ZSH weakened, and the characteristic peaks of MnO_2 began to appear. When fully charged to 1.80 V, an obvious characteristic peak of MnO_2 (310) was observed at $2\theta=28.7^\circ$. After completely discharged to 0.80 V again, the characteristic peaks of ZSH were obvious, which proved that the battery had good reversibility [31]. However, the signals of ZnMn_2O_4 and MnOOH were weak throughout, and the characteristic peaks were multiple at $2\theta=35^\circ\text{--}40^\circ$, so it was difficult to distinguish their signals. The weak signals of ZnMn_2O_4 and MnOOH were due to Mn^{3+} being unstable and prone to disproportionation reactions, so it was further transformed into Mn^{2+} and dissolved in electrolyte containing MnSO_4 [32,33].

For the ex-situ XPS spectra, in the high resolution of O 1s (Fig. 8(b)), the peak intensity of the Mn—O bond increased with the charged state and reached the strongest intensity when it was fully charged to 0.80 V. Figure 8(c) shows the high resolution of Mn 3s and Zn 3p. As the charge degree increased, the position of the Mn 3s double peaks gradually approached, which proved that the average oxidation state of Mn rose [34]. When fully charged to 0.80 V, the double-peak $dE \approx 4.7$ eV, which demonstrated that Mn^{4+} was dominant at this time. When completely discharged to 1.80 V, the double-peak $dE \approx 5.5$ eV, which proved that Mn^{2+} accounted for the largest proportion [31]. This was mutually confirmed that the Mn^{3+} converted into Mn^{2+} after disproportionation, as inferred by XRD.

In the ex-situ SEM images (Fig. 9), some phenomena consistent with those inferred by XRD and XPS were observed. When the traditional coating cathode was discharged to 1.27 V, some corrugated nanoarrays began to appear (Fig. 9(a)). The electrode surface was covered by a larger flaky substance after being discharged to 0.80 V

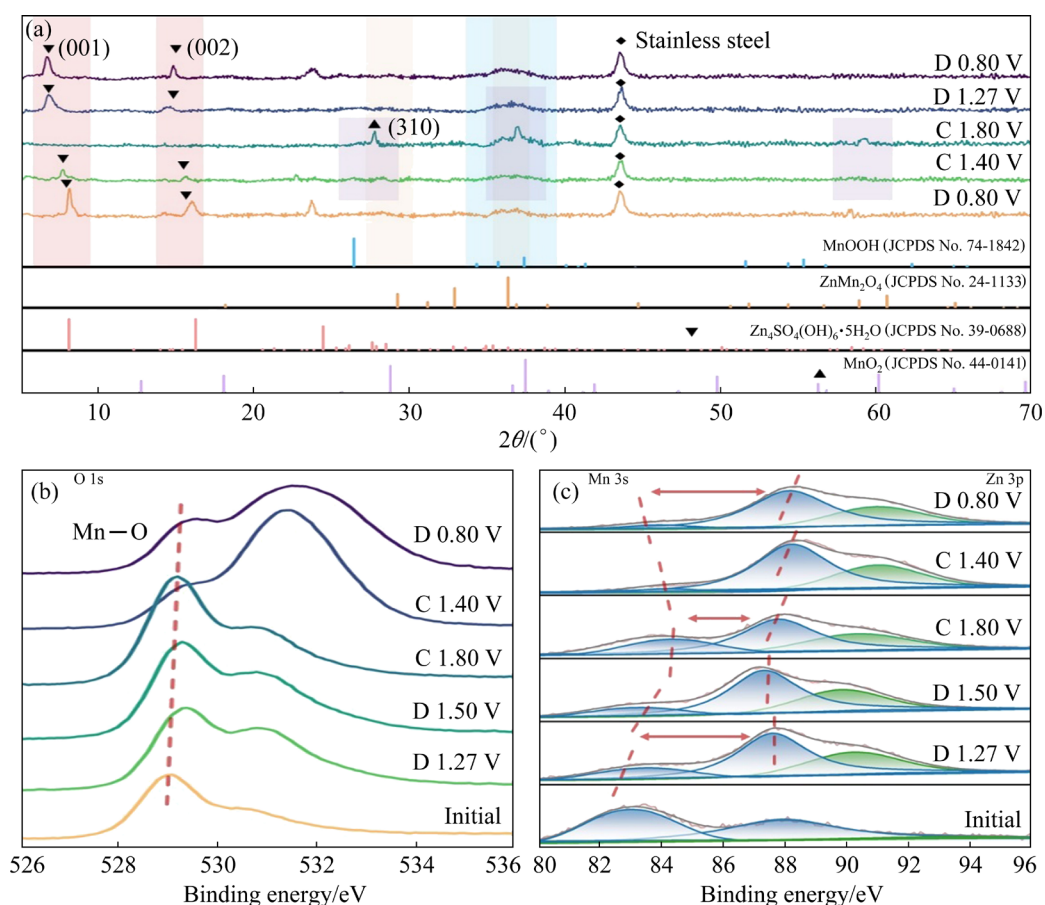


Fig. 8 Ex-situ XRD patterns at 100 mA/g (a), and ex-situ XPS spectra of O 1s (b) and Zn 3p/Mn 3s (c) of cathode (C—Charge; D—Discharge)

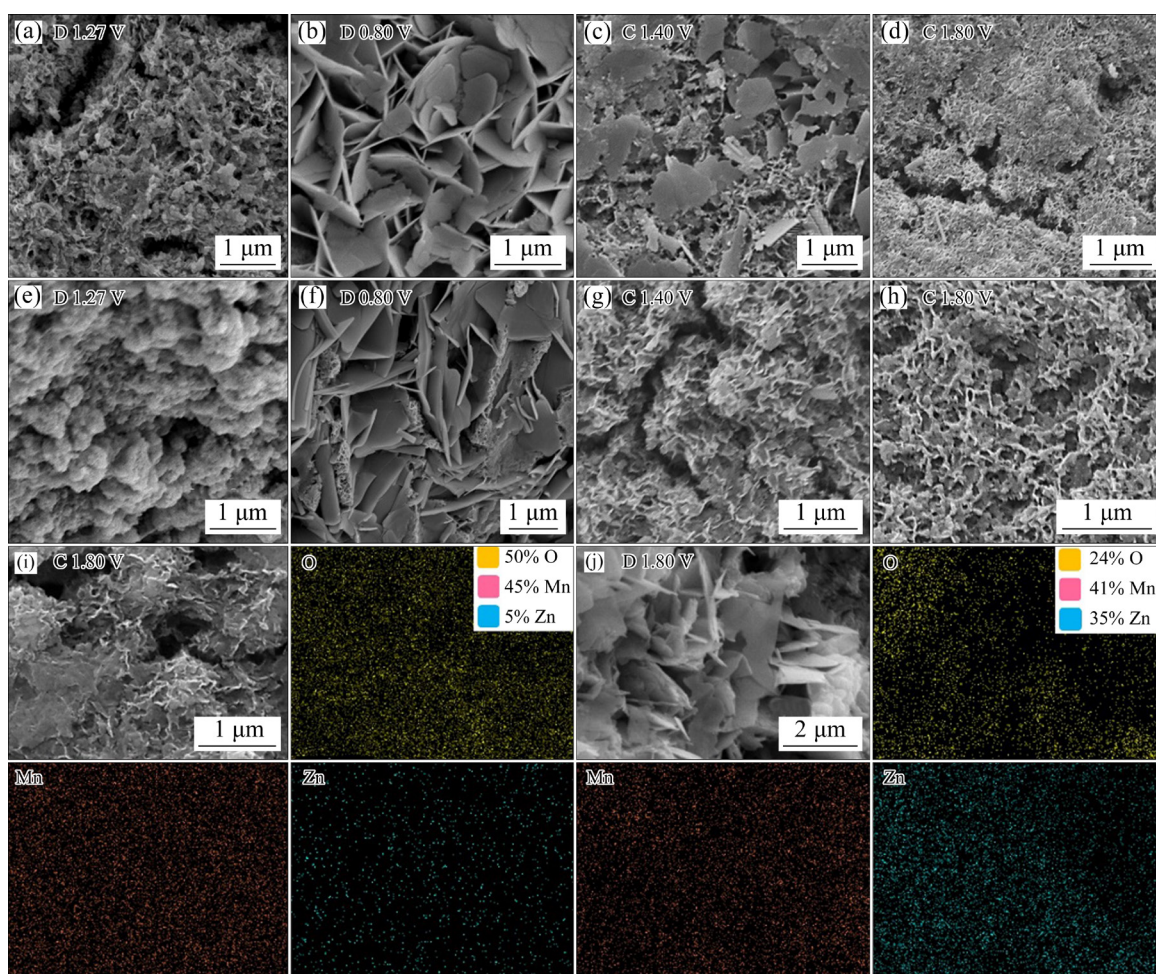


Fig. 9 Ex-situ SEM images of traditional coating cathode (a–d) and 3D printing cathode (e–h) at different states; EDX elemental mapping images of 3D printing cathode at different states (i, j) (C—Charge; D—Discharge)

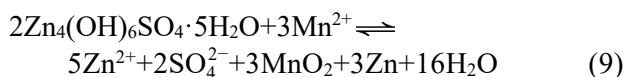
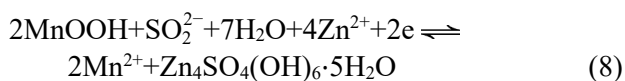
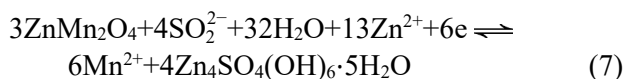
(Fig. 9(b)). When charged to 1.40 V, the two structures of nanosheets existed at the same time (Fig. 9(c)). Finally, the larger flakes disappeared at 1.80 V (Fig. 9(d)). When the 3D printing cathode was discharged to 1.27 V, the corrugated structure was relatively smaller (Fig. 9(e)). After being discharged to 0.80 V, the surface of the electrode was covered by a larger flaky substance, but part of the corrugated nanoarray could still be observed (Fig. 9(f)). After being fully charged (1.80 V), the corrugated structure deepens, and a higher specific surface area was provided (Fig. 9(h)).

The EDX elemental mapping images (Figs. 9(i, j)) show that Mn and O were evenly distributed on the surface of the 3D printing cathode when charged to 1.80 V, and the content of Zn was extremely low. After complete discharge, the content of Zn increased sharply and was evenly distributed in the flake-like parts, while Mn was mainly distributed in the gaps of the flakes. The

flaky substance prevented part of the active material from participating in the reaction after being covered. Combined with Fig. 8(a), the larger flaky substance was ZSH, while the corrugated structure was composed of MnO_2 , ZnMn_2O_4 and MnOOH in different proportions. The ratio of MnO_2 and the corrugated structure increased with the degree of charging. And one of the reasons for the good cycle stability of the 3D printing cathode was the thorough electrochemical reaction on the cathode.

Therefore, combined with the above analysis, it was speculated that there were three processes in the battery: the conversion of MnO_2 , MnOOH and ZnMn_2O_4 to $\text{Zn}_4\text{SO}_4(\text{OH})_6 \cdot 5\text{H}_2\text{O}$, the disproportionation of Mn^{3+} , and the dissolution/deposition of Mn^{2+} [35–37]. And the energy storage mechanism of the battery was described as follows:





Anode side:



As MnSO_4 was added to the electrolyte to provide plenty of Mn^{2+} in the system, the balance of Mn^{2+} moved to the deposition direction. As the number of cycles increased, MnO_2 particles gradually coarsened, which was confirmed in Figs. 4(g–i).

Besides, the solid liquid interface is the place of electrochemical reaction, which is equivalent to a good filtering device to transfer energy in a smooth way and has a significant influence on the reaction rate. Since the specific surface of the unit volume of the 3D printed electrode is four times that of the traditional electrode (Fig. 7(b)), the 3D printed electrode has a smoother oxidation–reduction reaction zone and a stable capacity retention capacity. Meanwhile, the mesh–layer structure adopted in this design provided a large amount of effective free space for volume contraction and expansion during the charge and discharge process and accelerated the diffusion of reaction heat, which significantly reduced the residual stress inside the electrode material.

4 Conclusions

(1) A high-accuracy customized 3D printed MnO_2 cathode was prepared via direct ink writing. The specific capacity of the 3D printing cathode was three times higher than that of the 2D cathode at 50 mA/g after 110 stable cycles.

(2) The cracking, peeling, and loss of active material caused by the residual stress in the material were reduced by the mesh-layer structure through 3D printing DIW. Therefore, DIW solves the problems of poor conductivity due to the shedding of current collectors, and optimizes the battery cycle performance.

(3) The pressure filtration effect was used to assist the extrusion process to improve the printing effect.

Acknowledgments

The financial support of the Natural Science Foundation of Changsha, China (No. kq2202094), and the National Key R&D Program of China (No. 2021YFB3701400), is greatly appreciated.

Supporting materials

Supporting materials in this paper can be found at: http://tmsc.csu.edu.cn/download/16-p1193-2022-0055-Supporting_materials.pdf.

References

- [1] ZHONG Cheng, LIU Bin, DING Jia, LIU Xiao-rui, ZHONG Yu-wei, LI Yuan, SUN Chang-bin, HAN Xiao-peng, DENG Yi-da, ZHAO Nai-qin, HU Wen-bin. Decoupling electrolytes towards stable and high-energy rechargeable aqueous zinc-manganese dioxide batteries [J]. *Nature Energy*, 2020, 5: 440–449.
- [2] ZHANG Li-shang, MIAO Ling, ZHANG Bao, WANG Jin-song, LIN Jia, TAN Qiu-yang, WAN Hou-zhao, JIANG Jian-jun. A durable $\text{VO}_2(\text{M})/\text{Zn}$ battery with ultrahigh rate capability enabled by pseudocapacitive proton insertion [J]. *Journal of Materials Chemistry A*, 2020, 8: 1731–1740.
- [3] LI Huan, CHAO Dong-liang, CHEN Biao, CHEN Xiao, CHUAH C, TANG You-hong, JIAO Yan, JARONIEC M, QIAO Shi-zhang. Revealing principles for design of lean-electrolyte lithium metal anode via in situ spectroscopy [J]. *Journal of the American Chemical Society*, 2020, 142: 2012–2022.
- [4] KUNDU D, VAJARGAH S H, WAN Li-wen, ADAMS B, PRENDERGAST D, NAZAR L F. Aqueous vs. nonaqueous Zn-ion batteries: Consequences of the desolvation penalty at the interface [J]. *Energy & Environmental Science*, 2018, 11: 881–892.
- [5] YANG Yong-qiang, TANG Yan, FANG Guo-zhao, SHAN Lu-tong, GUO Jia-sheng, ZHANG Wen-yu, ZHOU Jiang, WANG Chao, WANG Liang-bing, LIANG Shu-quan. Li^+ intercalated $\text{V}_2\text{O}_5 \cdot n\text{H}_2\text{O}$ with enlarged layer spacing and fast ion diffusion as an aqueous zinc-ion battery cathode [J]. *Energy & Environmental Science*, 2018, 11: 3157–3162.
- [6] CUI Jin, GUO Zhao-wei, YI Jin, LIU Xiao-yu, WU Kai, LIANG Peng-cheng, LI Qian, LIU Yu-yu, WANG Yong-gang, XIA Yong-yao, ZHANG Jiu-jun. Organic cathode materials for rechargeable zinc batteries: Mechanisms, challenges, and perspectives [J]. *ChemSusChem*, 2020, 13: 2160–2185.
- [7] FENG Ting-ting, YANG Jian, DAI Si-yi, WANG Jun-chao, WU Meng-qiang. Microemulsion synthesis of $\text{ZnMn}_2\text{O}_4/\text{Mn}_3\text{O}_4$ sub-microrods for Li-ion batteries and their conversion reaction mechanism [J]. *Transactions of Nonferrous Metals Society of China*, 2021, 31: 265–276.
- [8] JIANG Yu-qi, BA De-liang, LI Yuan-yuan, LIU Jin-ping. Noninterference revealing of “Layered to Layered” zinc storage mechanism of $\delta\text{-MnO}_2$ toward neutral Zn–Mn batteries with superior performance [J]. *Advancement of*

- Science, 2020, 7: 1902795.
- [9] ZHANG Kai, KIM D, HU Zhe, PARK M, NOH G, YANG Y, ZHANG Jing, LAU V W, CHOU Shu-lei, CHO M, CHOI S Y, KANG Y M. Manganese based layered oxides with modulated electronic and thermodynamic properties for sodium ion batteries [J]. *Nature Communications*, 2019, 10: 5203.
- [10] CHEN Cong, SHI Min-jie, ZHAO Yue, YANG Cheng, ZHAO Li-ping, YAN Chao. Al-intercalated MnO₂ cathode with reversible phase transition for aqueous Zn-ion batteries [J]. *Chemical Engineering Journal*, 2021, 422: 130375.
- [11] CAO Xian-wen, XU Yu-ting, YANG Bo, LANG Hong-zhi, SHEN Ze-xiang, WANG Ning, WANG Xiao-feng, WANG Sheng-han, SUN Cheng-lin. In-situ co-precipitated α -MnO₂@2-methylimidazole cathode material for high performance zinc ion batteries [J]. *Journal of Alloys and Compounds*, 2022, 896: 162785.
- [12] CHAO Dong-ling, QIAO Shi-zhang. Toward high-voltage aqueous batteries: Super- or low-concentrated electrolyte? [J]. *Joule*, 2020, 4: 1846–1851.
- [13] FANG Guo-zhao, ZHU Chu-yu, CHEN Ming-hui, ZHOU Jiang, TANG Bo-ya, CAO Xin-xin, ZHENG Xu-sheng, PAN An-qiang, LIANG Shu-quan. Suppressing manganese dissolution in potassium manganate with rich oxygen defects engaged high-energy-density and durable aqueous zinc-ion battery [J]. *Advanced Functional Materials*, 2019, 29: 1808375.
- [14] YU Xin-yao, LOU Xiong-wen. Mixed metal sulfides for electrochemical energy storage and conversion [J]. *Advanced Energy Materials*, 2018, 8: 1701592.
- [15] WANG Jian-gan, LIU Hong-zhen, SUN Huan-huan, HUA Wei, WANG Hu-wei, LIU Xing-rui, WEI Bing-qing. One-pot synthesis of nitrogen-doped ordered mesoporous carbon spheres for high-rate and long-cycle life supercapacitors [J]. *Carbon*, 2018, 127: 85–92.
- [16] MURAT C, KAKARLA R R, FERNANDO A M. Advanced electrochemical energy storage supercapacitors based on the flexible carbon fiber fabric-coated with uniform coral-like MnO₂ structured electrodes [J]. *Chemical Engineering Journal*, 2017, 309: 151–158.
- [17] TAO Si-jia, WANG Xiao-feng, ZENG Jing, YI Bing, PENG Chao-qun, WANG Ri-chu. Lattice materials and its fabrication by 3D printing: A review [J]. *The Chinese Journal of Nonferrous Metals*, 2022, 32: 416–444. (in Chinese)
- [18] CAI Xing-ke, LUO Yu-ting, LIU Bi-lu, CHENG Hui-ming. Preparation of 2D material dispersions and their applications [J]. *Chemical Society Reviews*, 2018, 47: 6224–6266.
- [19] WANG Hao-ran, GUO Rui-sheng, LI Hao-dong, WANG Jin-jin, DU Cheng-feng, WANG Xiao-long, ZHENG Zi-jian. 2D metal patterns transformed from 3D printed stamps for flexible Zn//MnO₂ in-plane micro-batteries [J]. *Chemical Engineering Journal*, 2022, 429: 132196.
- [20] ZHANG Guan-hua, ZHANG Xian-an, LIU Huai-zhi, LI Jin-hao, CHEN Yi-qin, DUAN Hui-gao. 3D-printed multi-channel metal lattices enabling localized electric-field redistribution for dendrite-free aqueous Zn ion batteries [J]. *Advanced Energy Materials*, 2021, 11: 2003927.
- [21] TAGLIAFERRI S, PANAGIOTOPOULOS A, MATTEVI C. Direct ink writing of energy materials [J]. *Materials Advances*, 2021, 2: 540–563.
- [22] LEWIS J A, Direct ink writing of 3D functional materials [J]. *Advanced Functional Materials*, 2006, 16: 2193–204.
- [23] LIU Zi-xian, TIAN Xiao-cong, LIU Min, DUAN Shan-shan, REN Ya-zhou, MA Hui, TANG Kang, SHI Jian-peng, HOU Shuen, JIN Hong-yun, CAO Guo-zhong. Direct ink writing of Li_{1.3}Al_{0.3}Ti_{1.7}(PO₄)₃-based solid-state electrolytes with customized shapes and remarkable electrochemical behaviors [J]. *Small*, 2021, 17: 2002866.
- [24] ZHANG Yan-an, LIU Yan-peng, LIU Zhen-hua, WU Xiao-guang, WEN Yu-xiang, CHEN Hang-da, NI Xia, LIU Guo-han, HUANG Juan-juan, PENG Shang-long. MnO₂ cathode materials with the improved stability via nitrogen doping for aqueous zinc-ion batteries [J]. *Journal of Energy Chemistry*, 2022, 64: 23–32.
- [25] WANG Xun, LI Ya-dong. Synthesis and formation mechanism of manganese dioxide nanowires/nanorods [J]. *Chemistry-A European Journal*, 2003, 9: 300–306.
- [26] WANG Xiao-feng, SUN Yue-hua, PENG Chao-qun, WANG Ri-chu, ZHANG Dou, MA Chao. Suspensions designed for direct ink writing [J]. *Journal of Inorganic Materials*, 2015, 30: 1139–1147.
- [27] CHEN Yi-ming, ZHOU Li-jie, WEI Jing, MEI Chang-tong, JIANG Shao-hua, PAN Ming-zhu, XU Chang-yan. Direct ink writing of flexible electronics on paper substrate with graphene/polypyrrole/carbon black ink [J]. *Journal of Electronic Materials*, 2019, 48: 3157–3168.
- [28] WEI Teng-sing, AHN B Y, GROTTO J, LEWIS J A. 3D printing of customized Li-ion batteries with thick electrodes [J]. *Advanced Materials*, 2018, 30: 1703027.
- [29] TIAN Xiao-cong, WANG Teng, MA Hui, TANG Kang, HOU Shuen, JIN Hong-yun, CAO Guo-zhong. A universal strategy towards 3D printable nanomaterial inks for superior cellular high-loading battery electrodes [J]. *Journal of Materials Chemistry A*, 2021, 9: 16086–16092.
- [30] LI Yun, WANG Shan-yu, SALVADOR J R, WU Jin-peng, LIU Bo, YANG Wan-li, YANG Jiong, ZHANG Wen-qing, LIU Jun, YANG Ji-hui. Reaction mechanisms for long-life rechargeable Zn/MnO₂ batteries [J]. *Chemistry of Materials*, 2019, 31: 2036–2047.
- [31] GUO Xun, ZHOU Jiang, BAI Chao-lei, LI Xin-kuo, FANG Guo-zhao, LIANG Shu-quan. Zn/MnO₂ battery chemistry with dissolution-deposition mechanism [J]. *Materials Today Energy*, 2020, 16: 100396.
- [32] WANG Ming-ming, ZHENG Xin-hua, ZHANG Xiang, CHAO Dong-liang, QIAO Shi-zhang, ALSHAREEF H N, CUI Yi, CHEN Wei. Opportunities of aqueous manganese-based batteries with deposition and stripping chemistry [J]. *Advanced Energy Materials*, 2020, 11: 2002904.
- [33] SUN Wei, WANG Fei, HOU S, YANG Chong-yin, FAN Xiu-lin, MA Zhao-hui, Gao Tao, HAN Fu-dong, HU Ren-zong, ZHU Min, WANG Chun-sheng. Zn/MnO₂ battery chemistry with H⁺ and Zn²⁺ coinserion [J]. *Journal of the American Chemical Society*, 2017, 139: 9775–9778.
- [34] ZHAO Shuai, HAN Bo, ZHANG Da-tong, HUANG Qun, XIAO Lei, CHEN Li-bao, IVEY D G, DENG Yi-da, WEI Wei-feng. Unravelling the reaction chemistry and degradation mechanism in aqueous Zn/MnO₂ rechargeable batteries [J]. *Journal of Materials Chemistry A*, 2018, 6:

- 5733–5739.
- [35] BLANC L E, KUNDU D, NAZAR L F. Scientific challenges for the implementation of Zn-ion batteries [J]. *Joule*, 2020, 4: 771–799.
- [36] HUANG Yong-feng, MOU Jian, LIU Wen-bao, WANG Xian-li, DONG Liu-bing, KANG Fei-yu, XU Cheng-jun. Novel insights into energy storage mechanism of aqueous rechargeable Zn/MnO₂ batteries with participation of Mn²⁺ [J]. *Nanomicro Lett*, 2019, 11: 49.
- [37] HUANG Jing-dong, ZENG Jing, ZHU Kun-jie, ZHANG Rui-zhi, LIU Jun. High-performance aqueous zinc-manganese battery with reversible Mn²⁺/Mn⁴⁺ double redox achieved by carbon coated MnO_x nanoparticles [J]. *Nanomicro Lett*, 2020, 12: 110.

水系锌离子电池 MnO₂ 正极的 3D 打印

刘真¹, 何汉兵¹, 罗泽湘¹, 王小锋², 曾婧¹

1. 中南大学 冶金与环境学院, 长沙 410083;
2. 中南大学 材料科学与工程学院, 长沙 410083

摘要: 为了解决 MnO₂ 正极在水系锌离子电池中循环稳定性差及离子运输缓慢等问题, 采用直写成型技术制备高精度定制的 3D 打印 MnO₂ 正极。流变测试表明, 打印墨水表现出剪切变稀行为, 存储模量平台值高达 10⁵ Pa。SEM 图像显示, 100 次循环后该定制网-层状结构保持完整。具有良好力学强度的 3D 结构有利于降低电极内残余应力, 同时提供更大的比表面积。所得的 3D 打印正极在 50 mA/g 的电流密度下循环 110 次后, 比容量为对照传统 2D 电极的 4 倍。采用多种非原位技术系统研究了 3D 打印电池的可逆 Mn²⁺/Mn⁴⁺ 双氧化还原储能机制。

关键词: α -MnO₂; 水系锌离子电池; 3D 打印; 直写成型; 储能机制

(Edited by Bing YANG)